AIChE

Estimation of Mass Transfer Velocity Based on Measured Turbulence Parameters

Johannes G. Janzen
Dept. of Environmental Engineering, Federal University of Rondônia, Jardim dos Migrantes, Ji-Paraná 76900-726, RO, Brazil

H. Herlina and Gerhard H. Jirka
Institute for Hydromechanics, University of Karlsruhe, Karlsruhe 76128, Germany

Harry E. Schulz
Nucleus of Thermal Engg. and Fluids, Dept. of Hydraulics and Sanitation, São Carlos School of Engineering, University of São Paulo, São Carlos 13560-970, SP, Brazil

John S. Gulliver
Dept. of Civil Engineering, University of Minnesota, Minneapolis, MN 55455

DOI 10.1002/aic.12123
Published online December 30, 2009 in Wiley InterScience (www.interscience.wiley.com).

The aim of this study is to quantify the mass transfer velocity using turbulence parameters from simultaneous measurements of oxygen concentration fields and velocity fields. The surface divergence model was considered in more detail, using data obtained for the lower range of β (surface divergence). It is shown that the existing models that use the divergence concept furnish good predictions for the transfer velocity also for low values of β, in the range of this study. Additionally, traditional conceptual models, such as the film model, the penetration-renewal model, and the large eddy model, were tested using the simultaneous information of concentration and velocity fields. It is shown that the film and the surface divergence models predicted the mass transfer velocity for all the range of the equipment Reynolds number used here. The velocity measurements showed viscosity effects close to the surface, which indicates that the surface was contaminated with some surfactant. Considering the results, this contamination can be considered slight for the mass transfer predictions. © 2009 American Institute of Chemical Engineers *AIChE J,* 56: 2005–2017, 2010
Keywords: laser-induced fluorescence, particle image velocimetry, air–water gas transfer, grid-stirred tank, mass transfer velocity

Introduction

Gas transfer across the air–water interface plays an important role in geophysical and industrial processes. A historical dominant interest lies in the transfer of oxygen from air to water, because the dissolved oxygen content of a body of water is a primary indicator of the water quality. However, the increase of industrial activity in the last century produced, as a consequence, the emission of large amounts of different gases and chemical compounds in the atmosphere and in water bodies. The interest in understanding the

Correspondence concerning this article should be addressed to J. G. Janzen at johannesjanzen@gmail.com.

underlying mechanisms of interfacial mass transfer was then directed to quantify transfer rates of a broader range of gases and compounds, such as carbon dioxide, methane, and volatile organic compounds, among others. Considering slightly soluble gases, where the liquid phase plays the dominant role, the study of oxygen absorption by water is convenient because the existing methods to measure concentrations and velocities permit to obtain insights about the general mechanisms that control mass transfer. Being essential to maintain life, the oxygen consumed in water bodies must be recovered, which occurs through the air–water interface. Thus, reoxygenation (or reaeration) should be carefully estimated. The mathematical models, which are used to quantify interfacial mass transfer, involve the turbulence level to which the interface is subjected. Considering the absence of bubbles and drops, the flux of gas, N, across the air–water interface is customarily expressed as

$$N = K(C_S - C_B), \tag{1}$$

where K is gas transfer velocity, which is applied to the transfer of volatile compounds and gases, C_S and C_B are the saturated and bulk concentration of the dissolved gas, respectively. An accurate value of K is needed to effectively predict gas transfer across the air–water interface. Although numerous conceptual theories have been proposed over the years (i.e., Lewis and Whitman,[1] Higbie,[2] Danckwerts,[3] Kishinevsky and Serebriansky,[4] Toor and Marchello,[5] Coantic,[6] and Schulz and Schulz[7]), the turbulence-related parameters in these theories are still poorly defined.

The theoretical predictions of interfacial mass transfer typically consider the one-dimensional form of the Fick's first law:

$$N = -D\left.\frac{dC}{dz}\right|_{\text{Interface}}, \tag{2}$$

where D is the molecular diffusivity of the dissolved gas in water and z denotes the vertical direction (with the convention that positive is in the downward direction).

In this study, some models were chosen to evaluate the mass transfer coefficient K (or transfer velocity). The models involve different parameters (or concepts) related to turbulence, permitting to compare predictions of K using these parameters (or combination of parameters). The film model by Lewis and Whitman[1] assumed that the transfer occurs only by molecular diffusion across a film of constant thickness. Outside of this film, the fluid is well mixed. It could be deduced that the liquid film coefficient is equal to

$$K = \frac{D}{\delta_c}, \tag{3}$$

where δ_c is the "film thickness," also named as the concentration boundary layer thickness, which must be quantified. Recognizing that the assumptions made for the (stagnant) film model would perhaps introduce errors in the quantification of K, Higbie[2] and Danckwerts[3] proposed that patches of the liquid surface are periodically replaced by fluid elements from the well-mixed bulk. Assuming that molecular gas transfer takes place for a certain time, after which the surface is renewed, which occur at a mean rate s, it can be shown that

$$K = \sqrt{Ds}, \tag{4}$$

where s is the mean surface renewal rate. The key problem in the penetration-renewal models lies in the prediction of s. After Higbie[2] and Danckwerts,[3] the models were more directed to relate surface renewal directly to measurable turbulence quantities. The large eddy model (Fortescue and Pearson[8]) and the small eddy model (Lamont and Scott[9]) are perhaps the best known of these models. In the large eddy model, for example, s is usually replaced by the ratio U/L, where U and L are the characteristic velocity and length of the larger eddies, respectively. The horizontal root-mean-square (rms) velocity, $\sqrt{\overline{u'^2}}$, and the length macroscale at the surface are common choices (Calmet and Magnaudet[10]), which lead to Eq. 5:

$$K \propto \left(\frac{D\sqrt{\overline{u'^2}}}{L}\right)^{1/2}. \tag{5}$$

As the dimension of s is the inverse of the time, Davies and Lozano[11] replaced s by the inverse of the time macroscale, T^{-1}, obtained from the autocorrelation function for velocities at the water surface.

McCready et al.[12] developed a technique for the quantification of K that relies upon the gradient of instantaneous velocity normal to the surface, $\beta' = dw/dz$, where w and z are the velocity component and coordinate normal to the surface, respectively. They used velocity measurements by Lau[13] near a solid surface, but outside of the concentration boundary layer, and assumed that these could apply near a free surface. Tamburrino and Gulliver[14] realized that β' could be measured at a free surface by applying the continuity equation (Eq. 6) and measuring u and v trough particle tracking.

$$\beta' = -\left(\frac{\partial u}{\partial x} + \frac{\partial v}{\partial y}\right). \tag{6}$$

The model permits to correlate turbulence parameters and mass transfer following a structured way. Various investigators have used a measured surface divergence to determine β' and predict K (Kumar et al.,[15] Law et al.,[16] Tamburrino and Gulliver,[17] Xu et al.,[18] and Tamburrino et al.[19]). Law and Khoo,[20] using CO_2 and water with different concentrations of glycerol (to obtain different Schmidt, $Sc = \nu/D$, numbers), proposed

$$K = 0.22\sqrt{\beta D}. \tag{7}$$

where β is the rms of β'. McKenna and McGillis[21,22] suggested that the surface divergence may also account for the presence of surface films. Considering contaminated surfaces, they presented the equation

$$K \cong 0.5\sqrt{\beta\nu}\,\mathrm{Sc}^{-n}$$
$$n = \begin{cases} 1/2 - \text{clean suraces} \\ 2/3 - \text{surfaces behave like a rigid wall} \end{cases} \tag{8}$$

where ν is the kinematic viscosity. Equation 8 may be viewed as a natural extension of the clean surfaces approach for slightly contaminated surfaces. It is not valid for strong

contamination, having in this case the same limitations mentioned by Hasegawa and Kasagi,[23] who studied contaminated surfaces quantified through the Weber and the Marangoni numbers, the last expressing the effect of surfactant concentrations on the surface tension. The authors performed numerical calculations using $\beta(t) = \beta \cos(\omega t)$ and presented the results as a function of β/ω. Different behaviors of the mass transfer were observed for values of β/ω higher or lower than 1. For highly contaminated surfaces, the mass transfer could not be quantified through the surface divergence, whereas clear and slightly contaminated surfaces correlate well with the single equation

$$K = 0.4\sqrt{\beta D}. \tag{9}$$

For clean surfaces, Eqs. 7–9 are equivalent except for the different coefficients. It can be noted that the important parameters governing the scalar transport for the clean surfaces are β and D. β is related to the hydrodynamics very close to the interface, and D is related to the species involved in interfacial transport. Equation 8 shows a distinction between clean and "rigid" contaminated surfaces, quantified through the additional parameter n. Additionally, to the effects of contamination on β directly, Eq. 8 proposes a correction using n when quantifying K. In this study, both proposals were considered (with and without n), reflecting the diverse views on the subject found in the literature.

One reason that analyses of gas transfer at a free surface have been slow in coming is the difficulty in making measurements near the free interface. The concentration boundary layer is usually of the order of 10- to 100-μm thick and is mobile, which makes measurements within the concentration boundary layer difficult, and limited in range of flow conditions. In the last 2 decades, laser-induced fluorescence (LIF) techniques have been used in studies of oxygen (O_2) transfer across air–water interfaces. A fluorescent dye, dissolved in water, fluoresces when excited by laser light. The fluorescence intensity is a function of the dye concentration and is measured with a CCD camera. The LIF technique allows the visualization of the concentration boundary layer, yielding far more detailed information than time-averaged mass transfer experiments (Jähne and Haussecker[24]). More recent attempts for the measurement of oxygen concentration fields near the air–water interface have been reported, for example, by Woodrow and Duke,[25] Lee,[26] Schladow et al.,[27] Herlina and Jirka,[28] Janzen et al.,[29] among others. Descriptions of experiments with simultaneous measurement of velocity and oxygen concentration in the near surface region are less frequent in the literature, which is probably related to the difficulty in obtaining results with a good resolution for both fields. Chu and Jirka[30] presented results obtained with a microprobe for concentration measurements and split-film anemometry for the turbulence measurements. Atmane and George[31] used a microprobe and polarographic methods for the concentration measurements and LDV for the velocity measurements. The authors furnish results for turbulent mass transfer, although mentioning the need of more accurate data. Herlina,[32] Janzen,[33] and Herlina and Jirka[34] presented measurements in which the LIF technique was used to measure the concentration field, and the particle image velocimetry (PIV) technique was used to measure the velocity field. Such combined measurements are needed to provide an understanding of the positive and negative mass fluxes inside the upper water layer, as emphasized by Atmane and George.[31]

This article presents results of measurements of both the concentration and the velocity fields near the air–water interface, using the nonintrusive LIF and PIV techniques. The concentration and velocity measurements were simultaneous. The dimensions of the velocity fields measured in this study were larger to those presented by Herlina and Jirka,[34] allowing observation of the interaction between the concentration and the velocity fields over larger distances. A comparison of the different concentration boundary layer thicknesses is made, and the parameters defined in different models of K are calculated within the lower range of β considered in this study.

Experimental Methods

Oscillating grid system

Figure 1a is a view of the oscillating-grid tank used in this study. The experiments were conducted in a tank made of Perspex, with a 0.50 m $\times$ 0.50 m square cross-section and 0.65 m height. A grid with 6.25-cm mesh size with a solidity of 36% was used, fulfilling the criteria of Hopfinger and Toly.[35] The grid was positioned 20.0 cm above the bottom of the tank to minimize secondary motion. The experiments were conducted at the Institute for Hydromechanics of the University of Karlsruhe, Germany, with a full description of the oscillating-grid tank given by Herlina[32] and Janzen.[33] The grid was operated with a 5.0 cm stroke S, and the frequency f varied from 2.0 to 5.0 Hz. The water depth above the grid, h, was maintained at 28.0 cm. The mean water temperature was 26.5°C. Data acquisition was begun 10 min after the onset of oscillation because the oscillating grid turbulence is sensitive to initial conditions (Cheng and Law[36]). All the experiments were performed in a single sequence, to guarantee similar environmental and surface conditions, and to permit comparisons between the data. Only the frequency was changed from one run to other. Table 1 presents experimental parameters, where Re is the Reynolds number defined for the experiments as fS^2/v.

Concentration measurements

A LIF technique was used to obtain dissolved oxygen concentration fields at the air–water interface. Pyrene butyric acid (PBA) was used as indicator for dissolved oxygen concentration in water (Vaughan and Weber[37]). The change in fluorescence lifetime, τ, and intensity, F (also called quenching) is quantitatively described by the Stern-Volmer equation:

$$\frac{F_0}{F} = \frac{\tau_0}{\tau} = 1 + K_{SV}C, \tag{10}$$

where F_0 and τ_0 are the fluorescence intensity and lifetime, respectively, in the absence of the quencher and K_{SV} is the Stern-Volmer quenching constant. Hence, the quencher concentration (in this case dissolved oxygen) can be determined by measuring the intensity of emitted fluorescence (in this case from PBA).

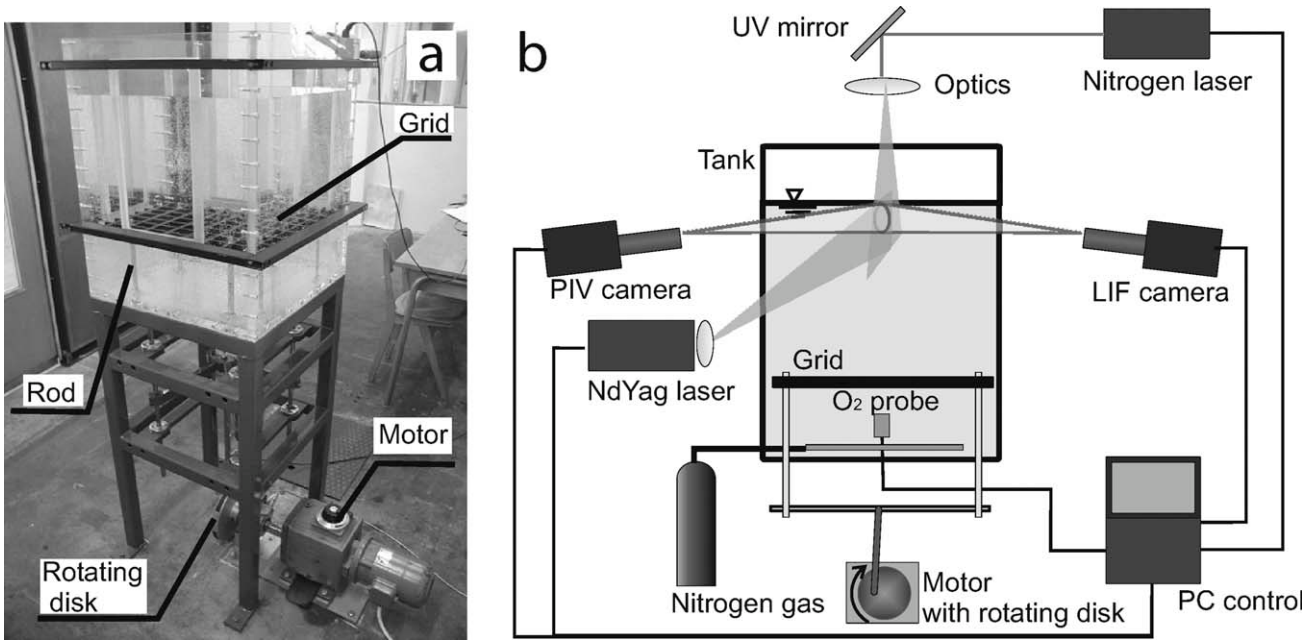

Figure 1. (a) Oscillating-grid tank (Herlina[32]); (b) experimental setup (Herlina[32]).

Figure 1b shows the LIF setup used in this study. The tank was filled with 2×10^{-5} mol/L PBA. The water in the tank was bubbled with nitrogen to remove oxygen through stripping. An initially dissolved oxygen concentration of about 0.7 mg/L was achieved after 20 min of bubbling. The experimental conditions imposed the saturation concentration at the interface during the experiments for a low solubility gas such as oxygen. A pulsed nitrogen laser (MNL 801) with a mean energy power of 0.4 mJ and a wavelength emission of 337.1 nm was used to excite the PBA solution. The laser beam was guided into the center of the tank through a UV-mirror and a combination of lenses. A FlowMaster CCD camera (1024 $\times$ 1280 pixels and 12 bit) with a macro-objective was used to obtain images of $\sim$9.5 mm $\times$ 11.9 mm from a distance of about 30 cm. The measurements have a resolution of $\sim$9 μm. The PBA fluorescence intensity lies between 370 and 410 nm. An optical bandpass filter was mounted in front of the camera to ensure that only the fluorescent light could pass through. The maximum number of successive images was limited to 300. Nine hundred images were taken for each run, which were averaged to obtain the temporally averaged field. This field was then horizontally averaged to obtain the average profiles. A series of image-processing steps were performed on the raw images, including noise removal, water surface detection, correction of laser attenuation, and correction of optical blurring near the interface. The image processing procedure followed the method described by Woodrow and Duke[25] and Herlina and Jirka.[28] The standard deviation of oxygen concentration images with the same concentration suggests that the resolution of the current setup is about 5%, as described by Herlina,[32] who used the same LIF setup of this study.

Table 1. Experimental Parameters

Run no.	f (Hz)	S (cm)	Re
1	2	5	5791
2	3	5	8687
3	4	5	11,582
4	5	5	14,478

Velocity measurements

The velocity field was measured using a PIV technique (Cheng and Law[36]). Figure 1b also shows the PIV setup used in this study. The light source was a 25 mJ NdYag laser. A CCD camera with a resolution of 1024 pixels $\times$ 1280 pixels was used to record the images. The field of view of the camera was 9.4 cm wide and 7.4 cm high. Polyamid particles with a nominal diameter of 10 μm were used as flow field tracers. After capturing and storing the images in the computer, the PIV software DaVis was applied to each pair of images (cross-correlation) to obtain velocity vector fields. The interrogation area chosen to evaluate the vectors was 0.23 cm $\times$ 0.24 cm (32 pixel $\times$ 32 pixels) with a 50% overlap. The size of the interrogation area affects data resolution, while the overlap of interrogation areas provides inherent correlations among the adjacent vectors. Nine hundred images were taken for each experiment run. Based on the technique described in Westerweel,[38] the accuracy (systematic error) of the current PIV system was evaluated to be less than 0.5 pixels (Herlina[32]).

Results and Discussion

Concentration boundary layer thicknesses

A normalized concentration, C^*, is used here to describe the behavior of the mean concentration in the concentration boundary layer, as

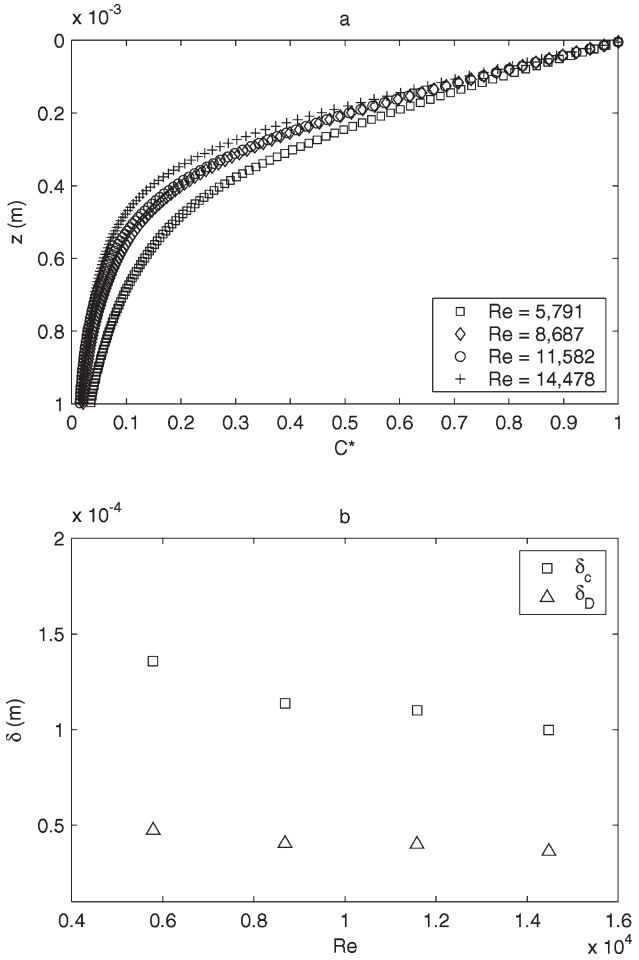

Figure 2. (a) Mean concentration profiles; (b) concentration boundary layer thickness and diffusive sublayer thickness vs. Reynolds number.

$$C^*(z) = \frac{\bar{C}(z) - C_B}{C_S - C_B}, \tag{11}$$

where $\overline{C}(z)$ is the mean gas concentration at distance z downward from water surface. The concentration boundary layer thickness, δ_c, is normally defined as the depth where the value of the normalized concentration C^* attains a value of 0.01, or

$$C^*(\delta_c) = \frac{\bar{C}(\delta_c) - C_B}{C_S - C_B} = 0.01. \tag{12}$$

The boundary layer is then the distance over which the gas concentration varies from the surface to 0.99 times the bulk value. Thinner than the concentration boundary layer, a region close to the surface is usually defined, within which eddy diffusion is slight compared to molecular diffusion. This region is called "diffusive sublayer," and throughout it the mean concentration profile evolves linearly (Magnaudet and Calmet[39]). Woodrow and Duke[25] presented a second definition of the concentration boundary layer, δ_D, as the intercept between the prolongation of the line determined by the concentration gradient at the water surface with the line which corresponds to the constant value of concentration, C_B:

$$\delta_D = \frac{C_S - C_B}{(-d\bar{C}/dz)|_{z=0}}. \tag{13}$$

Considering an exponential profile for C^* (Chu and Jirka[30]), the position $z = \delta_D$ implies that the concentration attains 0.63 times the bulk liquid value ($1/e$). As δ_D is obtained considering the linear part of the concentration profile, it is referred here as "diffusive sublayer." The instantaneous fluctuations around the mean concentration can be used to calculate rms profiles. Schulz and Schulz[7] showed that a peak of less than 0.5 must exist for the normalized rms curves of the concentration fluctuations, σ_c^*, defined as follows:

$$\sigma_c^* = \frac{\sqrt{\overline{[C(z) - \bar{C}(z)]^2}}}{C_S - C_\infty}. \tag{14}$$

Lee and Luck,[40] Atmane and George,[31] Herlina,[32] and Janzen[33] presented experimental results for σ_c^*.

Evolution of mean concentration along the depth

The nondimensional mean concentration profiles are shown in Figure 2a. These profiles are the result of a two-step process: (1) a mean profile for each image (or time step) was obtained, and (2) the so obtained 900 profiles were averaged along time. As expected, the profiles for higher turbulence conditions have steeper gradients close to the surface than those for lower turbulence conditions. The profiles permitted calculation of the boundary layer thickness for each run, as defined by Eq. 12, and the diffusive sublayer thickness, as defined by Eq. 13. A display of the concentration boundary layer thickness against Reynolds number is furnished in Figure 2b, showing that the boundary layer thickness is thinner for higher turbulent conditions. Figure 2b additionally shows the diffusive sublayer thickness against the Reynolds number, which is also thinner for higher agitation. This is a direct consequence of the steeper gradients at higher Reynolds number. For mean of the present data, $\delta_D \sim 0.36\delta_c$. All values are presented in Table 2.

Evolution of standard deviation along the depth

Concentration. Figure 3 presents the normalized rms concentration profiles, σ_c^*, as defined by Eq. 14. The profiles highlight two facts: (a) the curves reach a maximum of $z^* = z/\delta_c$ between 0.27 and 0.30, with an average value of 0.29; and (b) the normalized maximum of σ_c^* ranges between 0.13 and 0.17. These values are similar to results obtained in other works (Lee and Luck[40] obtained maximum σ_c^* between about 0.06 and 0.3, Atmane and George[31] obtained values between 0.2 and 0.3, Magnaudet and Calmet[39] obtained values between 0.28 and 0.35 for different Schmidt numbers, and Herlina[32] obtained values between 0.14 and 0.18) and are lower than the theoretical limit of 0.5.

The peak position, here denoted by δ_σ, is close to the surface, and numerical simulations performed by Magnaudet

Table 2. Measured Parameters

Re	5791	8687	11,582	14,478
Boundary layer thickness, δ_c (m) ($\times 10^{-3}$)	1.359	1.137	1.099	0.9973
Diffusive layer thickness (Eq. 13), δ_D (m) ($\times 10^{-4}$)	4.730	4.040	4.000	3.630
Diffusive layer thickness (peak of Eq. 14), δ_σ (m) ($\times 10^{-4}$)	4.082	3.108	3.108	2.922
Distance over which $\sqrt{\overline{w'^2}}$ is linear, Λ (m) ($\times 10^{-3}$)	9.86	9.86	8.70	8.70
Horizontal rms velocity, $\sqrt{\overline{u'^2}}$ (m/s) ($\times 10^{-3}$)	1.59	3.26	3.76	5.06
Vertical rms velocity difference $\Delta\sqrt{\overline{w'^2}}$ (m/s) ($\times 10^{-3}$)	1.48	2.66	2.26	3.31
Surface divergence, $\beta = \Delta\sqrt{\overline{w'^2}}/\Lambda$ (s^{-1})	0.15	0.27	0.26	0.38
Undisturbed length macroscale, L_u (m) ($\times 10^{-2}$)	3.37	3.92	3.31	3.63
Disturbed length macroscale, L_d (m) ($\times 10^{-2}$)	6.65	5.31	5.70	4.93
Time macroscale, T (s)	9.24	5.08	1.89	6.08

and Calmet[39] showed that it occurs near the edge of the so called "outer diffusive layer." The space between the surface and the peak position may be considered as the region where the free surface has a stronger influence, whereas the space "under" the peak position may be considered as the region where turbulence of the bulk liquid has a stronger influence. The mean position of the peak of σ_c^* is $\delta_\sigma = 0.29\delta_c$, which is close to $\delta_D = 0.36\delta_c$. For this set of experiments $\delta_\sigma = 0.80\delta_D$, on average (the coefficient is in the range of 0.77–0.86). It is possible to use δ_σ as indicator of the distance along which diffusive effects are important. This may be more representative, because δ_σ represents the effect of turbulent fluctuations and concentration gradient. All values are presented in Table 2.

Velocity. Figure 4 shows the variation of rms turbulent horizontal and vertical velocities with depth. The horizontal velocity, u_{rms}, shows characteristics similar to the results of Brumley and Jirka,[41] with some profiles forming a "bulge" in the surface influenced region and indicating a viscous boundary layer. The increase in the horizontal intensity outside of the influence of the viscous layer, while the vertical intensity, w_{rms}, decreases rapidly, is a result of the redistribution of the kinetic energy from the vertical motion to the horizontal motion, as shown experimentally by Law et al.[16] and theoretically by Hunt and Graham[42] and Magnaudet.[43] The horizontal and vertical velocities for the Reynolds numbers 8687 and 11,582 have almost the same value near the interface. A possible reason for this result may be the formation of circulation regions (secondary circulations or mean flow) whose geometrical characteristics changed from one agitation condition to the other, affecting the velocity values in the measurement region. Secondary circulations are present in oscillating grid-stirred turbulence, as pointed by McKenna and McGillis.[44]

At the surface ($z = 0$) the vertical rms velocity values must equal zero, relative to the location of the free surface.

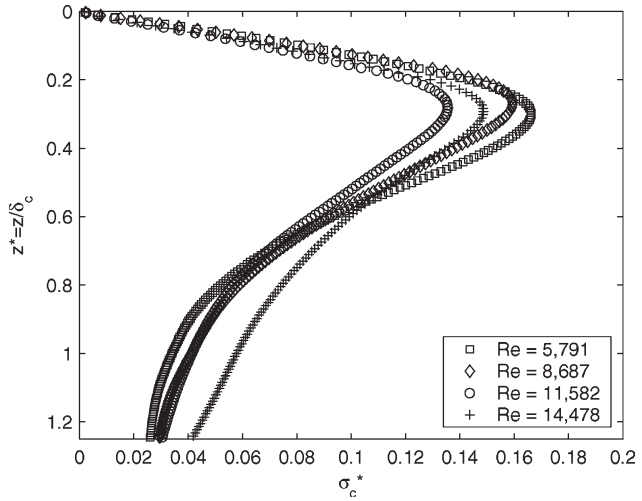

Figure 3. Variation of rms (root-mean-square) concentration with depth.

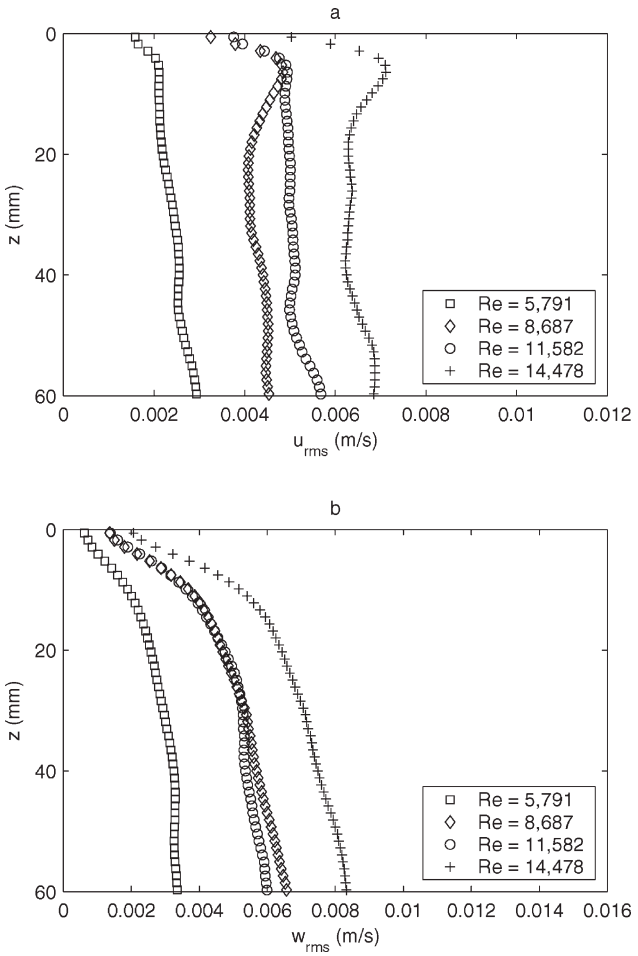

Figure 4. Variation of rms (root-mean-square) turbulent (a) horizontal and (b) vertical velocities with depth.

The values different from zero shown in Figure 4b are due to the resolution of the PIV measurements, in which velocities are evaluated within an interrogation area. In this case, the obtained "surface velocities" include distances until about 2.4 mm under the surface, where vertical velocity components still exist. Despite this bias at the surface, the profiles of the vertical rms velocity show a "quasi-linear" range until a distance of about 10 mm from the surface, which agrees with the hypothesis of McCready et al.[12] in the surface divergence models. Furthermore, the linear portion of the rms vertical velocity corresponds to the viscous boundary layer, which following the estimation from Brumley and Jirka,[41] should range between $z/z_s = 0.4$ and 0.6 (where z_s is the distance from the center of the stroke toward the water surface, or the average grid depth). In this study, it corresponds to $z/z_s = 0.4$. The linear regression R is greater than 0.99. Values of the rms velocities at the surface and along the region of linear variation are important in different models that predict K. The values of the rms velocities $\sqrt{\overline{u'^2}}$ (horizontal rms value at the surface) and $\Delta\sqrt{\overline{w'^2}}$ (difference between the extreme values of the vertical rms values in the linear region) are shown in Table 2, together with Λ (the distance along which the linear evolution of the vertical rms velocity holds) and β, which was calculated directly from $\beta = \Delta\sqrt{\overline{w'^2}}\Big/\Lambda$.

Nondimensional rms profiles of the horizontal and vertical velocity fluctuations are shown in Figure 5. The measured rms velocities are scaled with their values at $z = 28$ mm, while z is normalized with L_∞ ($L_\infty = 0.1z_s$). Brumley and Jirka[41] found that within a distance of ~10% of z_s from the surface, the velocity fluctuations are influenced by the surface. In this study, it corresponds to the used value of 28 mm. It can be observed that the normalized vertical fluctuation profiles superimpose along all the depth, whereas the horizontal fluctuation profiles are differently influenced by the surface, spreading out close to the surface. The solid lines, in Figure 5, are theoretical profiles proposed by Hunt and Graham,[42] obtained with parameters shown by Brumley and Jirka.[41] The shape of the measured and theoretical profiles agrees well for the vertical velocities. However, for the horizontal velocities, the observed behavior deviates from the theoretical curves close to the surface, with the experimental velocity values being lower than the theoretical values. The results of Brumley and Jirka[41] and Herlina and Jirka[34] showed similar behaviors.

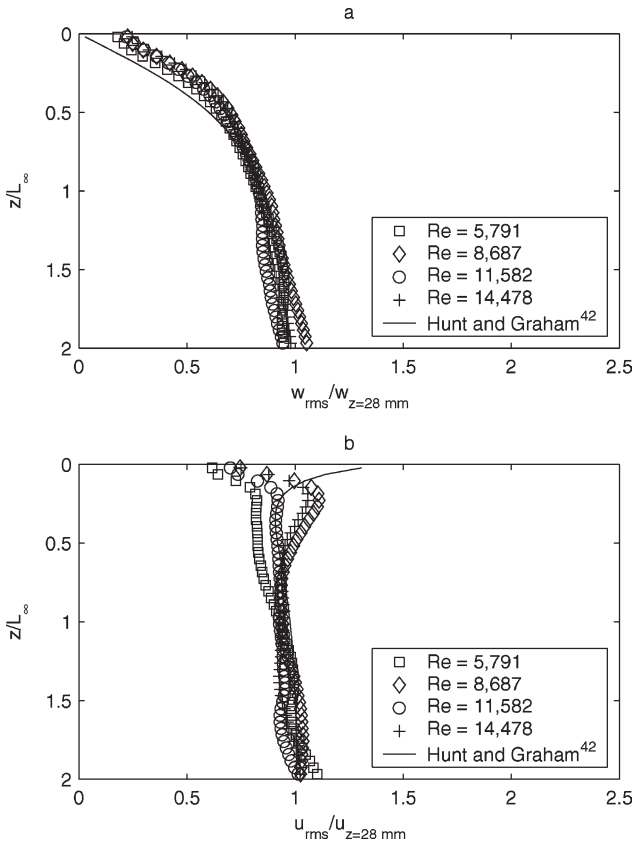

Figure 5. Vertical turbulence fluctuations near the interface.

(a) Vertical fluctuation and (b) horizontal fluctuation.

Evolution of integral length scales along the depth

Velocity Integral Length Scales. Length scales of turbulence are important to understand the change in shape of a typical eddy as it interacts with the free surface. To obtain the integral length scale, the correlation functions must be calculated. For two dimensional data, the correlations functions in the horizontal and vertical directions follow the same definition:

$$R_i^{[k]}(r) = \frac{\overline{v_i^{[k]'}(x).v_i^{[k]'}(x+r)}}{v_i^{[k]}(x) \cdot v_i^{[k]}(x+r)}, \tag{15}$$

where v_i' is the fluctuation either of u or w (horizontal and vertical velocity components), v_i is the rms value either of u' or w', i and k are the directions (x or z), and r is a distance vector. Once R_i is calculated, the correspondent length scale is calculated as follows:

$$L_i^{[k]} = \int_0^\infty R_i^{[k]}(r)dr_k. \tag{16}$$

Because there are two integral scales for each direction (x and z), a total integral length scale was calculated for each direction:

$$L^{[x]} = \sqrt{2(L_x^{[x]})^2 + (L_z^{[x]})^2} \tag{17}$$

$$L^{[z]} = \sqrt{2(L_x^{[z]})^2 + (L_z^{[z]})^2}. \tag{18}$$

The total horizontal and vertical integral length scales are plotted against the distance z in Figure 6, which shows that the vertical integral length scale decreases toward the interface, whereas the horizontal integral length scale increases toward the interface. This presents eddies that "flatten out" undergoing a reduction in their vertical extent and an increase in their horizontal extent. This reduction-increasing behavior is quantified, in this study, through factors in the range 1.7–2.7, which are close to the values of 2.0–3.0 found by Handler et al.[45]

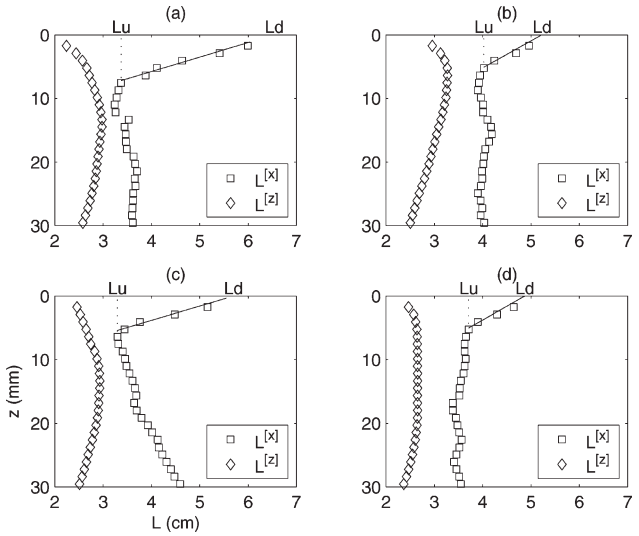

Figure 6. Profiles of velocity integral length scales, with linear curve fit of the expansion of $L^{[x]}$ near the surface.

(a) $Re = 5791$, (b) $Re = 8687$, (c) $Re = 11{,}582$, and (d) $Re = 14{,}478$.

The integral length scales are not constant within the region of measurement. Furthermore, there are two main scales to consider: horizontal and vertical. Therefore, it is difficult to define a characteristic value for a "length macroscale" close to the surface. Within the region shown in Figure 6, the vertical scale, $L^{[z]}$, for each run has a mean value between 2 and 3 cm, whereas the horizontal scale, $L^{[x]}$, has a mean value between 3 and 5 cm. As the effect of the surface on the horizontal scale is clearly shown (the abrupt distortion at the upper part of all runs shown in Figure 6), it seems reasonable to register the length just before the "flatten out" effect as an "undisturbed" characteristic horizontal length scale, L_u, as also adopted by Hunt and Graham[42] and Calmet and Maganudet.[46] In this case, this characteristic value falls within the interval from 3.4 to 4.0 cm (Figure 6). Additionally, the width of the flattened eddies at the surface may be used as a measure of the "disturbed" horizontal length scale, L_d. For the present set of experiments, this "disturbed" length falls within the interval from 4.9 to 6.7 cm. Figure 6 also shows straight lines fitting the points of the disturbed regions, which allows linear extrapolation to the surface. All values of undisturbed and disturbed length scales are shown in Table 2. Brumley and Jirka[41] suggested, on the basis of the Hunt and Graham[42] theory, that a purely kinematic effect of the surface is expected to extend over one integral length scale, $L_\infty = 0.1 z_s$ from the surface, which corresponds to the surface influenced layer. The same "undisturbed" length scale was also adopted by Calmet and Magnaudet.[46] In the present set of experiments, the average grid depth was maintained constant at 28 cm, which results in $L_\infty = 2.8$ cm. It is interesting to see that the "undisturbed" horizontal length scale oscillates between the limits of 3.32 and 3.92 cm (mean value of 3.56 cm), which may be compared to L_∞ and to the values of $(0.8–0.96)L_\infty$ found by Calmet and Magnaudet.[46]

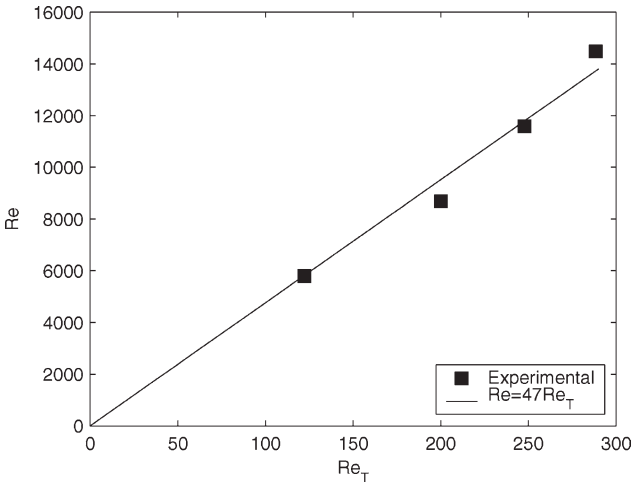

Figure 7. Proportionality between Re_T and Re.

The macroscales permit calculation of the "turbulence Reynolds number" at the surface, obtained with the horizontal rms velocity scale and the disturbed length scale $\left(Re_T = \sqrt{\overline{u'^2}} L_d / \nu\right)$. Figure 7 shows that Re_T is proportional to the equipment Reynolds number, Re, permitting the use of the latter as a measure of turbulence at the interface, where $Re = 47 Re_T$ on average.

The linkage of surface turbulence to the bulk turbulence of course depends on the equipment used to generate turbulence, a reason to directly measure superficial parameters to quantify mass transfer. The proportionality presented in Figure 7, however, shows that oscillating grid systems allow a good control of the superficial turbulence conditions.

Concentration Integral Time Scale. The concentration time scale is a measure of the average time during which the concentration persists with the same characteristics at a point of the space. The correlation function of concentration with respect of time is defined as follows:

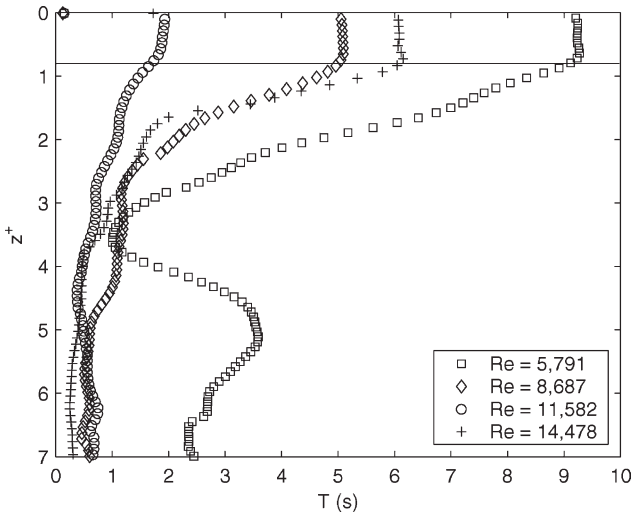

Figure 8. Profiles of concentration time scale ($z^+ = z/\delta_D$).

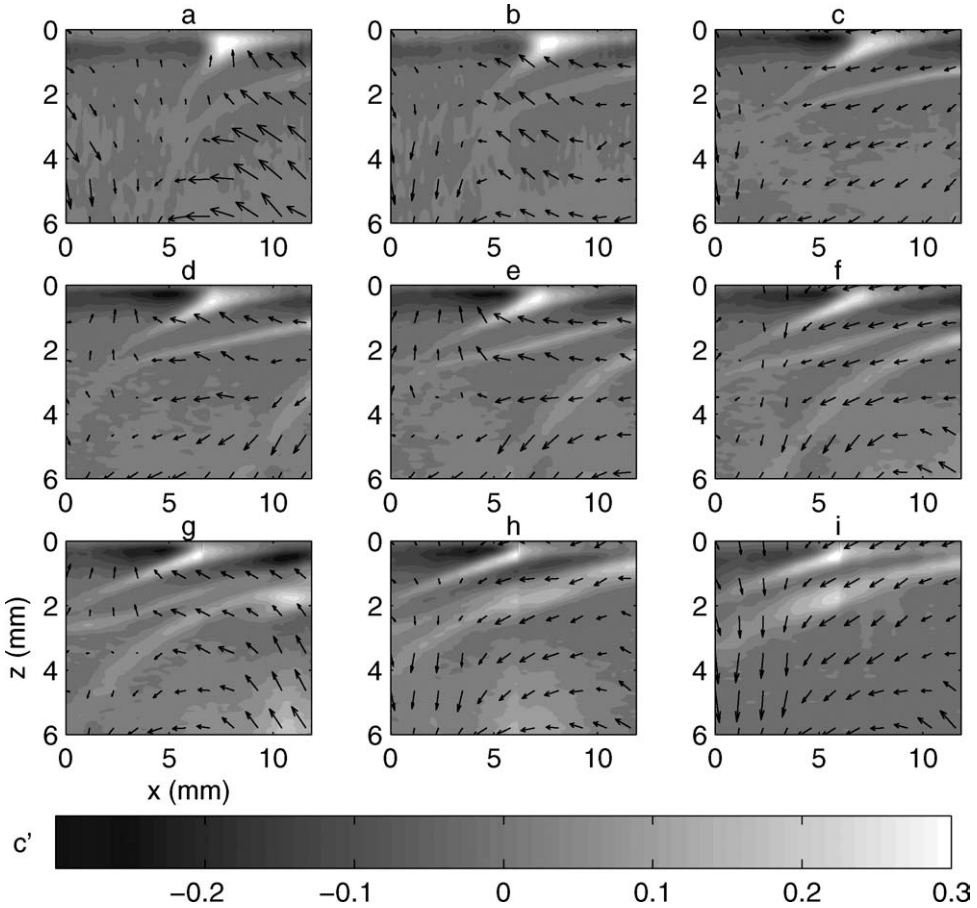

Figure 9. Sequence of instantaneous fluctuating oxygen concentration fields and related fluctuating vertical velocity fields.

The images were recorded at 4 Hz. In this figure, however, only every second recorded image is shown, thus the time interval between the shown images is 0.50 s. The reported fields are typically 12 mm × 6 mm.

$$R_c(\xi) = \frac{\overline{c_i'(t) \cdot c_i'(t+\xi)}}{c_i(t) \cdot c_i(t+\xi)}, \tag{19}$$

where c' is the fluctuation of concentration, c is the rms concentration, and ξ is a delay time. Once R_c is calculated, the correspondent time scale is calculated as follows:

$$T(z) = \int_0^{\Theta} R_c(t) d\xi|_z, \tag{20}$$

where Θ is the measurement time. R_c always reached the value 0 before attaining Θ. The measured concentration fields permit calculation of the time macroscale for each position along the z axis, which generates a function $T(z)$, as shown by Eq. 20. Figure 8 shows $T(z)$ along the normalized distance $z^+ = z/\delta_D$. All profiles indicate a high and approximately constant $T(z)$ in most of the diffusive sublayer. Figure 8 also shows a horizontal line, which indicates the position $z = 0.80\delta_D$. It can be seen that the integral time scale is relatively constant above this line, which corresponds to the mean value of δ_σ. Figure 8 incorporates three independent means of obtaining length scales related to the diffusive phenomena: (a) the vertical axis is presented in nondimensional form, using δ_D, obtained from the mean concentration profiles; (b) the horizontal line shows the mean value of δ_σ, obtained from the rms profiles for concentration fluctuations; and (c) the length of the region, where T is nearly constant, is close to both δ_D and δ_σ, and is obtained integrating autocorrelation functions (Eqs. 19 and 20). The present measurements therefore show a well-defined layer, consistently reproduced using the intersection of the concentration gradient, δ_D, the peak of the relative concentrations fluctuations, δ_σ, and the integration of the autocorrelation functions. Farther from the surface, the concentration time scale tends to decrease.

The time scale close to the surface decreases from 9.24 to 1.89 s for Reynolds numbers increasing in the range from 5791 to 11,582. An unexpected behavior is observed for the Reynolds number of 14,478, which shows a time scale of 6.08 s close to the surface. Considering the trend obtained for the lower Reynolds numbers, a value less than 1.89 s was expected for $Re = 14{,}478$. As the fluctuating velocities for this Reynolds number show a coherent behavior of the rms values (Figure 4), a possible reason would be changes in the conditions of the mean flows, such as secondary circulation. To observe the mean flows in detail, a larger region of measurement would be necessary. All values of the time macroscales are shown in Table 2.

Table 3. Predictions of the Mass Transfer Velocity (m/s)

Column	1	2	3	4	5	6	7
		Film model, Eq. 3 using		Penetration-renewal model (Eq. 4 using $s = T^{-1}$, after Davies and Lozano[11])		Divergence model using	
Re	K_{ref}, Eq. 21	δ_c	δ_σ		Large eddy model, Eq. 5	Eq. 7	Eq. 8, $n = 0.613$
5791	5.58*	1.81	6.05	16.3	7.77	4.23	4.97
8687	6.54	2.16	7.95	22.1	12.3	5.68	6.66
11,582	6.55	2.24	7.95	36.2	12.8	5.58	6.54
14,478	7.23	2.46	8.45	20.2	15.9	6.74	7.90

*Mass transfer velocity values must be multiplied by 10^{-6}.

Simultaneous visualization of velocity and concentration fields

Figure 9 presents examples of instantaneous concentration and vertical velocity fields, allowing visualization of the transport of oxygen at the water side of the interface. The origin of the vertical axis, z, is located at the water surface. Note that portions of the surface layer with high oxygen concentration are peeled off by a turbulent structure and then transported into the bulk region. The resolution of the images for the concentration fields is better than that for the velocity fields. Notwithstanding this resolution difference, it is seen that the evolution of the concentration fields is closely related to the vertical velocity fields. In other words, the observed distortions of the concentration ''spots'' are coupled with the observed movements of the liquid.

The concentration fields' evolution in Figure 9 indicates a clear horizontal movement directed from right to left, which coincides with the direction indicated by the velocity vectors. It is known that the vertical velocity is zero at the surface, but the resolution used for the velocity fields imposed a higher velocity value at the surface. Considering pictures c, f, h, and i, the vertical velocity components at the surface ($z = 0$) are mainly directed from the surface to the bottom. Pictures a, b, c, f, h, and i show a clear descending movement in the left side, also seen in the lower left quarter of the remaining pictures, which transports the parcels of liquid with higher oxygen concentration deeper into the liquid. Pictures g, h, and i show an ascendant movement on the right side, which implies in a thinning of the surface region with higher oxygen concentration, as expected. It is seen that the general form of the concentration records, with a deeper penetration into the liquid on the left side of the pictures, and a horizontal movement from right to left, is consistent with the velocity fields recorded at the same time. However, a complete description of the flow and the concentration fields can only be obtained with a three-dimensional visualization of the subsuperficial region.

Using measured parameters to quantify the gas transfer velocity

Combining Eqs. 1 and 2, the mass transfer coefficient K (or transfer velocity) can be directly estimated in this study, following the equation

$$K_{ref} = \frac{-D\left.\frac{dC}{dz}\right|_{z=0}}{C_S - C_B} = \frac{D}{\delta_D}. \quad (21)$$

The gradient, $dC/dz|_{z=0}$, is a linear fit based on the maximum slope of the concentration profile near the interface. The transfer velocities estimated using Eq. 21 are shown in column 1 of Table 3 (reference K). The measured turbulence parameters (Table 2) were used to compare predictions of K from different models with the reference K, from Eq. 21. The molecular diffusivity D and water kinematic viscosity ν at 26.5°C were adopted as 2.47×10^{-9} and 8.63×10^{-7} m^2/s, respectively (Janzen[33]).

The results of β (Table 2) and K_{ref} (column 1, Table 3) permit comparison of the present data with the surface divergence models. Figure 10 follows the graphs of Xu et al.,[18] where $K(D\beta)^{-1/2}$ is plotted against β. The shadowed areas correspond to the data of McKenna and McGillis[22] and those used by Xu et al.[18] The data of Tamburrino and Gulliver,[17] Tamburrino et al.,[19] Tamburrino and Aravena,[47] Herlina and Jirka,[34] and Xu et al.[48] are plotted together with the present results. It can be observed that the data from Herlina and Jirka[34] are comparable to the present data, although the transfer velocity was determined through long-time oxygen concentration measurements in the bulk liquid. For the present set of data, the mean coefficient of Eq. 7 is 0.26, which is close to the coefficient 0.22 of Law and Khoo.[20] The predictions obtained with Eq. 7 are shown in column 6 of Table 3. As Figure 4a indicates the presence of viscous effects

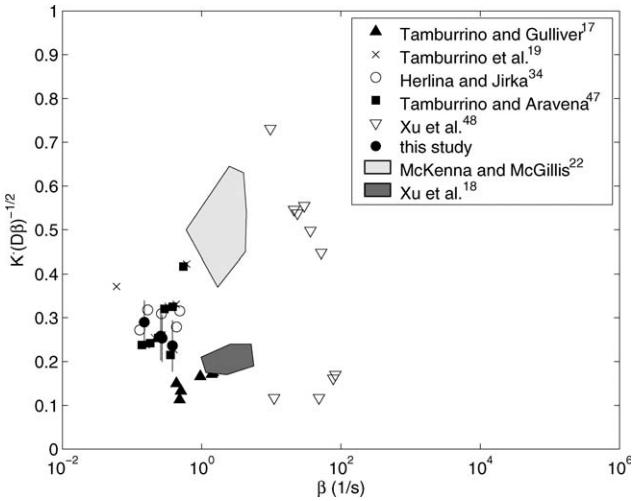

Figure 10. $K(D\beta)^{-1/2}$ plotted against β, evidencing data obtained for the lower range of β.

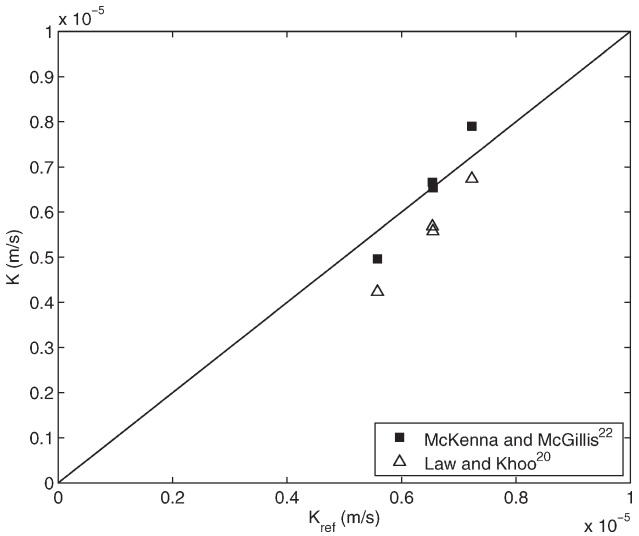

Figure 11. Comparison of the predictions obtained from Eqs. 8 (McKenna and McGillis[22]) and 9 (Law and Khoo[20]) with measured data.

Equation 8 was used with $n = 0.613$.

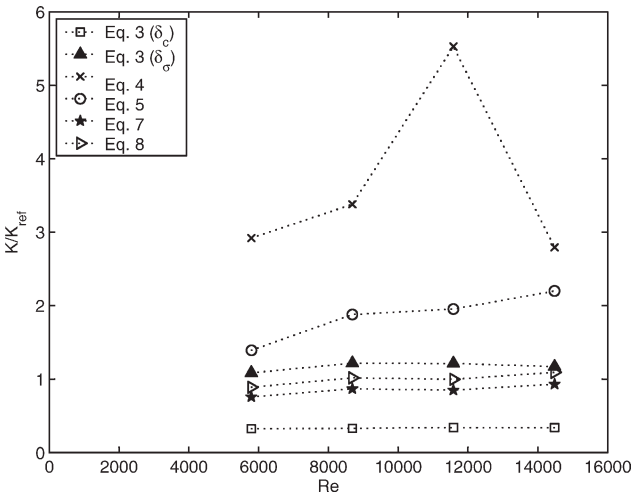

Figure 12. Ratio K/K_{ref} against Re, showing that predictions which consider the film thickness and the superficial divergence maintain a constant proportionality with K_{ref}.

Equation 8 was used with $n = 0.613$.

near the surface, the observed maintenance of values close to predictions of Eq. 7 suggests that the contamination of the surface is "slight," in the sense described by Hasegawa and Kasagi.[23] Equation 8 (McKenna and McGillis[22]) needs the value of n to permit predictions. The use of Eq. 8 also implies that the experimental value of n must be between the limits of 1/2 and 2/3. A best fit procedure was followed (least square method) between the predictions of Eq. 8 and the reference K, and the value $n = 0.613$ was obtained, which satisfies the suggested limits. The exponent $n \approx 0.613$ found to fit Eq. 8 suggests that the surface is contaminated, especially when compared with the results of McKenna and McGillis.[22] This is consistent with the reduction of the horizontal rms velocity displayed in Figures 4 and 5, and is a possible reason for the lower values of the rms concentration normalized maximum presented in Figure 3, when compared with the results of Magnaudet and Calmet.[39]

The predictions of Eq. 8 using the best fit value of n are shown in column 7 of Table 3. Figure 11 shows measured and predicted results of K, using the divergence models.

It is known that $\delta_c = \delta_c(D)$, which would change the exponent of D in the stagnant film model and introduce new variables. However, measured values of vertical scales for the concentration field already consider the effects of D in their results, so the film model may be used with the different vertical scales measured here. Columns 2 and 3 of Table 3 show the results obtained for K using δ_c and δ_σ, respectively. Column 2 evidences the fact that the usual definition of boundary layers (like Eq. 12) overestimates the "film thickness" used in Eq. 3. Column 3 shows agreement with column 1, a consequence of the similarity between δ_σ and δ_D. Considering Eq. 4 and the Davies and Lozano[11] model (time macroscale at the surface replaces s^{-1}), the values of K reported in column 5 of Table 3 are obtained. The measured time scales are too small to fit the reference K values without a proportionality coefficient. A similar conclusion was also reported by Davies and Lozano.[11] Considering Eq. 5 with the horizontal scales of velocity and length right at the surface (Calmet and Magnaudet[10]), the values of K reported in column 6 are obtained. In this case, Eq. 5 already predicts the need of a proportionality coefficient.

If predicted and measured K are proportional, the ratio K/K_{ref} will be constant for the different agitation conditions. Figure 12 shows K/K_{ref} obtained from Table 3 against the Reynolds number. Different behaviors are observed for different predictions. The predictions of Eq. 4 oscillate strongly. The predictions of Eq. 5 behave smoother than those of Eq. 4, but K/K_{ref} increases significantly with the Reynolds number, which implies that probably not all details of the mass transfer phenomena are captured by this model. The predictions of Eq. 3 and the length scales δ_c and δ_σ show K/K_{ref} nearly constant, suggesting that both scales can be used to predict K, provided that the proportionality coefficient is known. The predictions obtained with Eqs. 8 and 9, the surface divergence models, show small variations in the ratio K/K_{ref} with the Reynolds number, also pointing to the convenience of their use to quantify K. In this case, Eq. 8 was already adjusted to the data ($n = 0.613$), which leads to $K/K_{ref} = 1$. The mean values of K/K_{ref} obtained with the present set of data are given in Table 4, which may be used in the respective predictive equations of K.

Table 4. Mean Values of K/K_{ref}

Equation referred in the text and in Figure 12	Observed K/K_{ref}
Eq. 3 (δ_c)	0.335
Eq. 3 (δ_σ)	1.176
Eq. 4 ($s = T^{-1}$)	No constant K/K_{ref} observed
Eq. 5	No constant K/K_{ref} observed
Eq. 8 ($n = 0.613$)	1.0
Eq. 9	0.864

Conclusions

Simultaneous PIV and LIF measurements were used to investigate the interaction between air–water gas transfer and turbulence generated in an oscillating-grid tank. The rms velocity profiles showed the usual damping of the vertical motion in interfacial regions, while the horizontal motion tends to increase. In this study, viscous effects were observed close to the surface, also partially damping the horizontal velocity fluctuations. This indicates that the surface was lightly contaminated by some surfactant. The velocity integral length scales reveal a significant flattening of a typical eddy near the air–water interface. This flattening is evidenced by a notably larger horizontal scale and a commensurately smaller vertical scale.

Considering the concentration measurements, vertical mean and rms concentration profiles were obtained from the concentration fields. The peak of the concentration fluctuation intensity profiles could be very well registered. The concentration time scale profiles showed an approximately constant value of the time macroscale in the diffusive sublayer. It was shown that the diffusive sublayer may be computed following different ways: using the mean concentration profile, the profile for the rms value of the concentration fluctuations, or the integral time scale, obtaining similar thicknesses.

A comparison was made between mass transfer velocities obtained directly from its definition (Eq. 21, used as reference) and using different models. The transfer velocities were quantified using turbulence parameters from the simultaneous concentration and velocity measurements. The surface divergence model was considered in more detail, with measured β values ranging from 0.15 to 0.38 (lower range of β). It is shown that the predictions of the equation of Law and Khoo[20] are close to the reference value of K; while a value of $n = 0.613$ permits the use of the equation of McKenna and McGillis,[22] where n satisfies the limits $1/2 < n < 2/3$. The comparisons show that, for the present experiments, predictions close to the reference mass transfer velocity were obtained using either the film model with the diffusive sublayer (δ_D, δ_σ) or the surface divergence models. The constancy of K/K_{ref} for the Reynolds number ranging from 5791 to 14,478 points to the good predictions of these models. From the obtained results, the contamination of the surface can be considered slight for the mass transfer predictions.

Acknowledgments

The authors are indebted to the Brazilian research support foundations CAPES (trough process 2201/06-2), CNPq, and FAPESP, for the support of different stages of this study, and to the "German Science Foundation" (DFG Grant No. Ji18/7-1).

Literature Cited

1. Lewis W, Whitman W. Principles of gas absorption. *Ind Eng Chem*. 1924;16:1215–1220.
2. Higbie R. The rate of absorption of a pure gas into a still liquid during short periods of exposure. *Am Inst Chem Eng*. 1935;31:365–390.
3. Danckwerts P. Significance of liquid film coefficients in gas absorption. *Ind Eng Chem*. 1951;43:1460–1467.
4. Kishinevsky M, Serebriansky M. The mechanism of mass transfer at the gas-liquid interface with vigorous stirring. *J Appl Chem-USSR*. 1955;29:29–33.
5. Toor H, Marchello J. Film-penetration model for mass and heat transfer. *AIChE J*. 1958;4:97–101.
6. Coantic M. A model of gas transfer across air-waters with capillary waves. *J Geophys Res*. 1986;91:3925–3943.
7. Schulz HE, Schulz SAG. *Modelling below-surface characteristics in water reaeration*. In: Wrobel LC, Brebbia CA, editors. *Water Pollution, Modelling, Measuring and Prediction*. Southampton, U.K.: Computational Mechanics, 1991:441–454.
8. Fortescue GE, Pearson JRA. On gas absorption into a turbulent liquid. *Chem Eng Sci*. 1967;22:1163–1176.
9. Lamont JC, Scott DS. An eddy cell model of mass transfer into the surface of a turbulent liquid. *AIChE J*. 1970;16:513–519.
10. Calmet I, Magnaudet J. High Schmidt number mass transfer through turbulent gas-liquid interfaces. *Int J Heat Fluid Flow*. 1998;19:522–532.
11. Davies J, Lozano F. Turbulence and surface renewal at the clean surface of a stirred vessel. *AIChE J*. 1984;30:502–504.
12. McCready MJ, Vassiliadou E, Hanratty TJ. Computer simulation of turbulent mass transfer at a mobile interface. *AIChE J*. 1986;32:1108–1115.
13. Lau KK. Study of turbulence structure close to a wall using conditional sampling techniques. Doctoral thesis, University of Illinois, Urbana, 1980.
14. Tamburrino A, Gulliver JS. Free-surface turbulence measurements in an open-channel flow. In: Rood EP, Katz J, editors. *Free-Surface Turbulence*. New York: ASME, 1994:103–112.
15. Kumar S, Gupta R, Banerjee S. An experimental investigation of the characteristics of free turbulence in channel flow. *Phys Fluids*. 1998;10:437–456.
16. Law CNS, Khoo BC, Chew TC. Turbulence structure in the immediate vicinity of the shear free air-water interface induced by a deeply submerged jet. *Exp Fluids*. 1999;27:321–331.
17. Tamburrino A, Gulliver JS. Free-surface turbulence and mass transfer in a channel flow. *AIChE J*. 2002;48:2732–2742.
18. Xu ZF, Khoo BC, Carpenter K. Mass transfer across the turbulent gas-water interface. *AIChE J*. 2006;52:3363–3374.
19. Tamburrino A, Aravena C, Gulliver JS. Visualization of 2-D divergence on free surface and its relation to gas transfer. In: Garbe CS, Handler RA, Jähne B, editors. *Transport at the Air-Sea Interface*. Berlin: Springer, 2007:73–86.
20. Law CNS, Khoo BC. Transport across a turbulent air-water interface. *AIChE J*. 2002;48:1856–1868.
21. McKenna SP, McGillis WR. *Surface divergence and air-water gas transfer*. In: McKenna SP, McGillis WR, Donelan MA, Drennan WM, Saltzman ES, Wanninkhof R, editors. *Gas Transfer at Water Surfaces. AGU Geophysical Monograph Series*, Vol. 127, AGU Press, 2002:129–134.
22. McKenna SP, McGillis WR. The role of free-surface turbulence and surfactants in air-water gas transfer. *Int J Heat Mass Transfer*. 2004;47:539–553.
23. Hasegawa Y, Kasagi N. *Turbulent mass transfer mechanism across a contaminated air-water interface*. In: Eaton, JK, Friedrich, R, Gatski, TB, Humphrey, JAC, editors. *4th International Symposium on Turbulence and Shear Flow Phenomena*, Williamsburg, VA, 2005: 971–976.
24. Jähne B, Haussecker H. Air-water gas exchange. *Annu Rev Fluid Mech*. 1998;30:443–468.
25. Woodrow PT Jr, Duke SR. *LIF measurements of oxygen concentration gradients along flat and wavy air-water interfaces*. In: McKenna SP, McGillis WR, Donelan MA, Drennan WM, Saltzman ES, Wanninkhof R, editors. *Gas Transfer at Water Surfaces. AGU Geophysical Monograph Series*, Vol. 127, AGU Press, 2002:83–88.
26. Lee M. Visualization of oxygen transfer across the air-water interface using a fluorescence oxygen visualization method. *Water Res*. 2002;36:2140–2146.
27. Schladow S, Lee M, Hürzeler B, Kelly P. Oxygen transfer across the air-water interface by natural convection in lakes. *Limnol Oceanogr*. 2002;47:1394–1404.
28. Herlina H, Jirka GH. Application of LIF to investigate gas transfer near the air-water interface in a grid-stirred tank. *Exp Fluids*. 2004;37:341–349.

29. Janzen JG, Schulz HE, Jirka GH. Air-water gas transfer details (Portuguese). *Revista Brasileira de Recursos Hídricos*. 2006;11:153–161.
30. Chu C, Jirka GH. Turbulent gas flux measurements below the air-water interface of a grid-stirred tank. *Int J Heat Mass Transfer*. 1992;35:1957–1968.
31. Atmane MA, George J. *Gas transfer across a zero-shear surface: a local approach.* In: McKenna SP, McGillis WR, Donelan MA, Drennan WM, Saltzman ES, Wanninkhof R, editors. *Gas Transfer at Water Surfaces*. *AGU Geophysical Monograph Series*, Vol. 127, AGU Press, 2002:255–259.
32. Herlina H. Gas transfer at the air-water interface in a turbulent flow environment. Doctoral thesis, Institute of Hydromechanics, University of Karlsruhe, 2005.
33. Janzen JG. Gas transfer near the air-water interface in an oscillating-grid tanks and properties of isotropic turbulent flows (Portuguese). Doctoral thesis, University of Sao Paulo, 2006.
34. Herlina H, Jirka GH. Experiments on gas transfer at the air-water interface induced by oscillating grid turbulence. *J Fluid Mech*. 2008;594:183–208.
35. Hopfinger E, Toly J. Spatially decaying turbulence and its relation to mixing across density interfaces. *J Fluid Mech*. 1976;78:155–175.
36. Cheng N, Law A. Measurements of turbulence generated by oscillating grid. *J Hydraul Eng*. 2001;127:201–208.
37. Vaughan W, Weber G. Oxygen quenching of pyrenebutyric acid fluorescence in water—a dynamic probe of the microenvironment. *Biochemistry*. 1970;9:464–473.
38. Westerweel J. Theoretical analysis of the measurement precision in particle image velocimetry. *Exp Fluids*. 2000;28:3–12.
39. Magnaudet J, Calmet I. Turbulent mass transfer through a flat shear-free surface. *J Fluid Mech*. 2006;553:155–185.
40. Lee Y, Luck S. Characterization of concentration boundary layer in oxygen absorption. *Ind Eng Chem Fundam*. 1982;21:428–434.
41. Brumley B, Jirka GH. Near-surface turbulence in a grid-stirred tank. *J Fluid Mech*. 1987;183:235–263.
42. Hunt JCR, Graham JMR. Free-stream turbulence near plane boundaries. *J Fluid Mech*. 1978;84:209–235.
43. Magnaudet J. High-Reynolds-number turbulence in a shear-free boundary layer: revisiting the Hunt-Graham theory. *J Fluid Mech*. 2003;484:167–196.
44. McKenna SP, McGillis WR. Observations of flow repeatability and secondary circulation in an oscillating grid-stirred tank. *Phys Fluids*. 2004;16:3499–3502.
45. Handler RA, Swean TF Jr, Leighton RI, Swearingen JD. Length scales and the energy balance for turbulence near a free surface. *AIAA J*. 1993;31:1998–2007.
46. Calmet I, Magnaudet J. Statistical structure of high-Reynolds-number turbulence close to the free surface of an open-channel flow. *J Fluid Mech*. 2003;474:355–378.
47. Tamburrino A, Aravena C. Reaeration coefficient determined from agitated water tank experiments. In: *5th International Conference on Hydroscience and Engineering*, Warsaw, Poland, 2002:255–259.
48. Xu ZF, Khoo BC, Wijeysundera NE. Mass transfer across the falling film: simulations and experiments. *Chem Eng Sci*. 2008;63:2559–2575.

Manuscript received Dec. 8, 2008, and revision received Oct. 17, 2009.